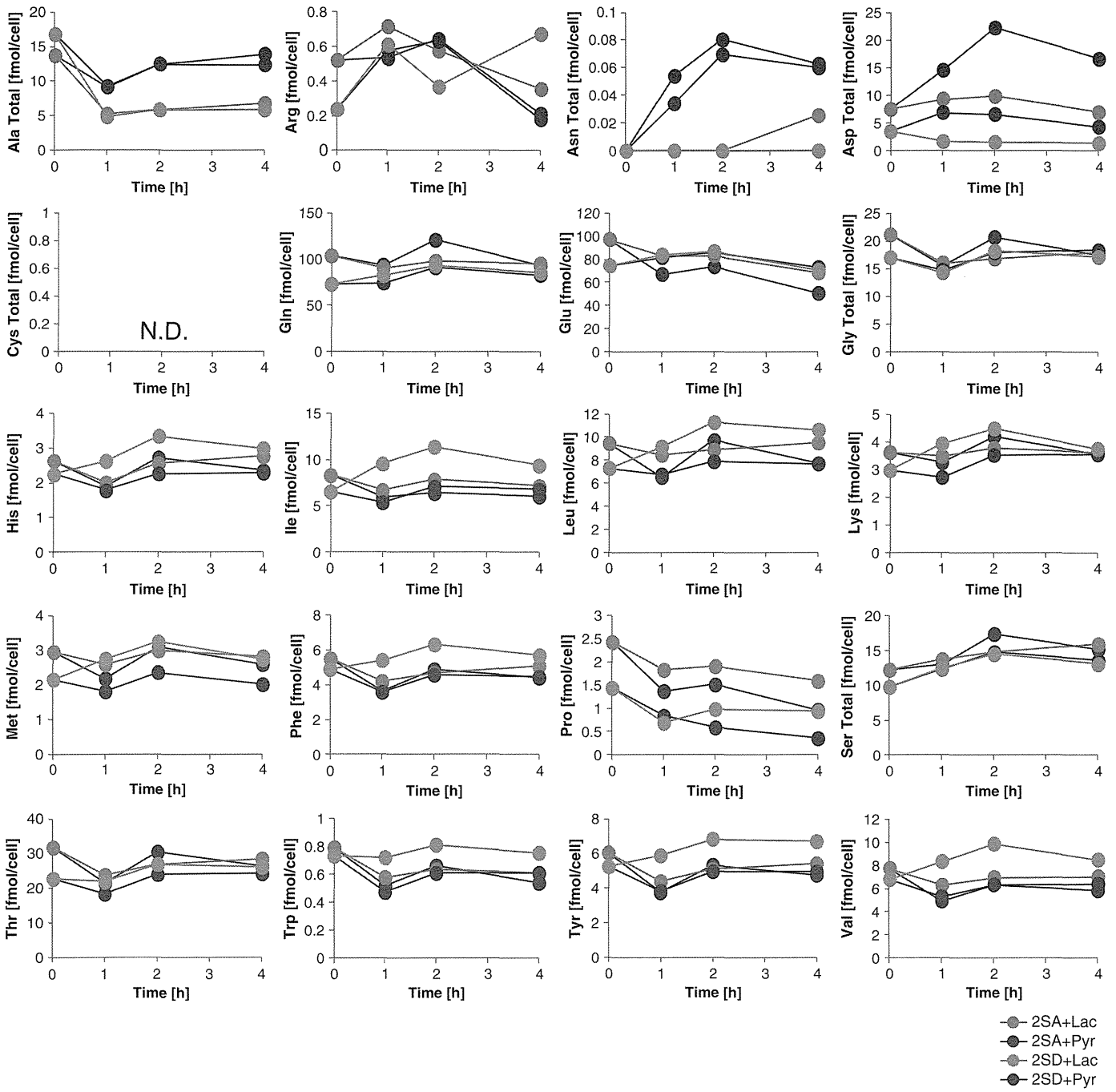

Fig. 4. Time-dependent changes in intracellular amino acid concentrations in 2SA and 2SD cells cultured with 10 mM lactate or 10 mM pyruvate. "N.D." indicates that the metabolite level was under the detection limit of CE-TOFMS analysis.

amino acids both intracellularly and in the medium. A high autophagic activity in 2SD cells can also be inferred by the increased production of reactive oxygen species (ROS) in MELAS syndrome (Rusanen et al., 2000), since ROS have been identified as signaling molecules to induce autophagy (Scherz-Shouval et al., 2007). In fact, the intracellular ROS level in 2SD cells is higher than that in 2SA cells (Fujita et al., 2007) and oxygen exposure-induced apoptosis is higher in MELAS mutant cells than in normal controls (Zhang et al., 1998). These findings thus imply that excessive ROS generated by the impaired respiratory chain facilitated autophagy in lactate-supplied 2SD cells, which eventually generated free amino acids and contributed to the increase in the levels of essential amino acids. In this perspective, the diminished accumulation of these essential amino acids in pyruvate-supplied 2SD cells may be explained by the fact that pyruvate is in fact a strong antioxidant and reacts with and reduces H_2O_2 (Desagher et al., 1997; Nath et al., 1995); thus, the pyruvate treatment might have alleviated oxidative stress and the accompanying autophagic activity in the 2SD cells.

Lactate is a well-known sensitive metabolic marker of MELAS (Castillo et al., 1995), which was also supported by its constantly high intracellular level and high increasing rate in the medium, as observed in this study. We also identified a few other metabolites that might function as potential MELAS markers. For example, the average increasing rate of medium Lys (Supplementary Fig. 3) in lactate-supplied 2SD cells (~171 fmol/cell/h) was significantly higher than that in the pyruvate-supplied 2SD cells (~53.7 fmol/cell/h) and 2SA cells (~33.8 fmol/cell/h under both lactate- and

pyruvate-supplied conditions). A possible reason for this high Lys level in the medium of the lactate-supplied 2SD cells might be the fact that the catabolism of Lys to acetyl CoA is known to involve 4 reactions that require NAD^+ as a cofactor; and thus this catabolic pathway may have been slowed down because of the constitutively low [NADH]/[NAD] ratio in the 2SD cells. Though to a lesser extent, a similar trend was observed in the increasing rate of Val in the medium (Supplementary Fig. 3; ~270 fmol/cell/h in lactate-supplied 2SD cells and ~202 fmol/cell/h under the other conditions). This may be again due to the shortage of NAD^+ in the lactate-supplied 2SD cells, as the catabolic pathway of Val to succinyl CoA is known to involve 3 reactions that require NAD^+ as a cofactor. The balanced [NADH]/[NAD] ratio seems critical also for the catabolism of these essential amino acids, since the increasing rate in these amino acids was lowered to the levels observed in 2SA cells by the pyruvate treatment. Although the overall trend of medium levels of Lys and Val appeared not to be considerably different among the conditions (Supplementary Fig. 3), this significant difference in the increasing rate of medium Lys and Val between the lactate-supplied 2SD cells and cells under the other conditions may be amplified in the long term. Accordingly, Lys and Val might be manifested in the blood or urine of MELAS patients and detectable as a diagnostic marker for MELAS and most likely other mitochondrial diseases showing imbalanced [NADH]/[NAD] as a pathologic condition. Moreover, gamma-aminobutyric acid (GABA) was one of the few metabolites that showed a clear cell line-specific trend independent of pyruvate- or lactate-administration (Supplementary Fig. 4). The intracellular GABA level in 2SA cells was nearly twice as high as that in 2SD cells throughout the experiment, and this trend was unchanged by either pyruvate or lactate treatment. Thus, GABA administration might be effective to somehow alleviate the symptoms of MELAS. Indeed, it has been speculated that treatment with inhibitory neurotransmitters such as GABA is theoretically effective to lower hyperexcitability in MELAS patients (Iizuka and Sakai, 2005).

Pyruvate administration does not always exhibit the expected efficacies in MELAS patients and not necessarily allow an optimistic outlook. This is perhaps by reason of the polygenetic nature of the cause of MELAS, which is known to be associated with at least 29 specific point mutations. There are at least 7 identified point mutations in the mitochondrial tRNA(Leu) gene, as well as mutations affecting many other mitochondrial tRNA genes (His, Lys, Gln, and Glu) and protein-coding genes (MT-ND1, MT-CO3, MT-ND4, MT-ND5, MT-ND6, and MT-CYB; (Sproule and Kaufmann, 2008)). Nevertheless, it is likely that the symptoms associated with lactic acidosis, *i.e.*, a high [NADH]/[NAD] ratio and possibly oxidative stress, would be alleviated by pyruvate administration. Current treatment regimens for MELAS patients involve indiscriminative administration of vitamins, cofactors, and oxygen-radical scavengers, which aims at the mitigation, postponement, or circumvention of the postulated damage to the respiratory chain (DiMauro and Schon, 2003). But pyruvate treatment could be a more effective, affordable, side effect-free, and most importantly, metabolically rational treatment regimen to improve symptoms associated with MELAS and even those of many other mitochondrial diseases. Such treatment would do so by facilitating efficient anaerobic glycolysis and probably supporting a limited but steady activity of oxidative phosphorylation for enhancing ATP production. Metabolome analysis of 2SA cells and MELAS mutant 2SD cells not only highlighted the basal metabolic differences between these cell lines but also their metabolic alterations and flux profiles in response to a high dose of lactate or pyruvate administration. The results showed a dramatic and sustainable effect of pyruvate administration on the energy metabolism of 2SD cells, supporting the idea that balancing the [NADH]/[NAD] ratio is crucial for facilitating anaerobic glycolysis for sufficient energy production in MELAS mutant cells. In this perspective, the efficacy of pyruvate treatment may not be limited to only alleviation of the symptoms associated with MELAS but rather also to that of those associated with a wider range of mitochondrial diseases.

Supplementary data to this article can be found online at http://dx.doi.org/10.1016/j.mito.2012.07.113.

Acknowledgments

The authors thank Dr. Masahiro Sugimoto for software development and Dr. Maria R. Monton and Ms. Kaori Igarashi for conducting the metabolome analysis. This work was supported in part by the following grants: a grant of the Global COE Program entitled, "Human Metabolomic Systems Biology," "Grant-in-Aid" research grants for the 21st Century Centre of Excellence (COE) Program (F-3); Scientific Research (A-22240072 and B-21390459), Creative Scientific Research (180 73004, 18GS0314), Targeted Proteins Research Program (TPRP), and Scientific Research on Priority Areas "Systems Genomes" and "Lifesurveyor" from the Ministry of Education, Culture, Sports, Science, and Technology (MEXT) of Japan; Grant-in-Aids (H23-016, H23-119, and H24-005) for the Research on Intractable Diseases (Mitochondrial Disease) from the Ministry of Health, Labour and Welfare (MHLW) of Japan; grants for scientific research from the Takeda Science Foundation; a grant for biological research from Gifu Prefecture, Japan; and research funds from the Government of Yamagata Prefecture and Tsuruoka City, Japan.

References

Castillo, M., Kwock, L., Green, C., 1995. MELAS syndrome: imaging and proton MR spectroscopic findings. AJNR Am. J. Neuroradiol. 16, 233–239.

Chomyn, A., Martinuzzi, A., Yoneda, M., Daga, A., Hurko, O., Johns, D., Lai, S.T., Nonaka, I., Angelini, C., Attardi, G., 1992. MELAS mutation in mtDNA binding site for transcription termination factor causes defects in protein synthesis and in respiration but no change in levels of upstream and downstream mature transcripts. Proc. Natl. Acad. Sci. U. S. A. 89, 4221–4225.

Desagher, S., Glowinski, J., Premont, J., 1997. Pyruvate protects neurons against hydrogen peroxide-induced toxicity. J. Neurosci. 17, 9060–9067.

DiMauro, S., Schon, E.A., 2003. Mitochondrial respiratory-chain diseases. N. Engl. J. Med. 348, 2656–2668.

Fujita, Y., Ito, M., Nozawa, Y., Yoneda, M., Oshida, Y., Tanaka, M., 2007. CHOP (C/EBP homologous protein) and ASNS (asparagine synthetase) induction in cybrid cells harboring MELAS and NARP mitochondrial DNA mutations. Mitochondrion 7, 80–88.

Goto, Y., Nonaka, I., Horai, S., 1990. A mutation in the tRNA(Leu)(UUR) gene associated with the MELAS subgroup of mitochondrial encephalomyopathies. Nature 348, 651–653.

Hasegawa, H., Matsuoka, T., Goto, Y., Nonaka, I., 1991. Strongly succinate dehydrogenase-reactive blood vessels in muscles from patients with mitochondrial myopathy, encephalopathy, lactic acidosis, and stroke-like episodes. Ann. Neurol. 29, 601–605.

Hirano, M., Pavlakis, S.G., 1994. Mitochondrial myopathy, encephalopathy, lactic acidosis, and strokelike episodes (MELAS): current concepts. J. Child Neurol. 9, 4–13.

Hirayama, A., Kami, K., Sugimoto, M., Sugawara, M., Toki, N., Onozuka, H., Kinoshita, T., Saito, N., Ochiai, A., Tomita, M., Esumi, H., Soga, T., 2009. Quantitative metabolome profiling of colon and stomach cancer microenvironment by capillary electrophoresis time-of-flight mass spectrometry. Cancer Res. 69, 4918–4925.

Hussein, A., Kasmani, R., Irani, F., Mohan, G., Ashmawy, A., 2009. An uncommon cause of lactic acidosis: MELAS. Eur. J. Intern. Med. 20, e114–e115.

Ichiki, T., Tanaka, M., Kobayashi, M., Sugiyama, N., Suzuki, H., Nishikimi, M., Ohnishi, T., Nonaka, I., Wada, Y., Ozawa, T., 1989. Disproportionate deficiency of iron-sulfur clusters and subunits of complex I in mitochondrial encephalomyopathy. Pediatr. Res. 25, 194–201.

Iizuka, T., Sakai, F., 2005. Pathogenesis of stroke-like episodes in MELAS: analysis of neurovascular cellular mechanisms. Curr. Neurovasc. Res. 2, 29–45.

Ishii, N., Nakahigashi, K., Baba, T., Robert, M., Soga, T., Kanai, A., Hirasawa, T., Naba, M., Hirai, K., Hoque, A., Ho, P.Y., Kakazu, Y., Sugawara, K., Igarashi, S., Harada, S., Masuda, T., Sugiyama, N., Togashi, T., Hasegawa, M., Takai, Y., Yugi, K., Arakawa, K., Iwata, N., Toya, Y., Nakayama, Y., Nishioka, T., Shimizu, K., Mori, H., Tomita, M., 2007. Multiple high-throughput analyses monitor the response of *E. coli* to perturbations. Science 316, 593–597.

Junker, B.H., Klukas, C., Schreiber, F., 2006. VANTED: a system for advanced data analysis and visualization in the context of biological networks. BMC Bioinforma. 7, 109.

Koga, Y., Povalko, N., Katayama, K., Kakimoto, N., Matsuishi, T., Naito, E., Tanaka, M., 2012a. Beneficial effect of pyruvate therapy on Leigh syndrome due to a novel mutation in PDH E1alpha gene. Brain Dev. 34, 87–91.

Koga, Y., Povalko, N., Nishioka, J., Katayama, K., Yatsuga, S., Matsuishi, T., 2012b. Molecular pathology of MELAS and l-arginine effects. Biochim. Biophys. Acta 1820, 608–614.

Komaki, H., Nishigaki, Y., Fuku, N., Hosoya, H., Murayama, K., Ohtake, A., Goto, Y., Wakamoto, H., Koga, Y., Tanaka, M., 2010. Pyruvate therapy for Leigh syndrome due to cytochrome c oxidase deficiency. Biochim. Biophys. Acta 1800, 313–315.

Liu, C.Y., Lee, C.F., Hong, C.H., Wei, Y.H., 2004. Mitochondrial DNA mutation and depletion increase the susceptibility of human cells to apoptosis. Ann. N. Y. Acad. Sci. 1011, 133–145.

Nath, K.A., Ngo, E.O., Hebbel, R.P., Croatt, A.J., Zhou, B., Nutter, L.M., 1995. alpha-Ketoacids scavenge H2O2 in vitro and in vivo and reduce menadione-induced DNA injury and cytotoxicity. Am. J. Physiol. 268, C227–C236.

Ohashi, Y., Hirayama, A., Ishikawa, T., Nakamura, S., Shimizu, K., Ueno, Y., Tomita, M., Soga, T., 2008. Depiction of metabolome changes in histidine-starved *Escherichia coli* by CE-TOFMS. Mol. Biosyst. 4, 135–147.

Pavlakis, S.G., Phillips, P.C., DiMauro, S., De Vivo, D.C., Rowland, L.P., 1984. Mitochondrial myopathy, encephalopathy, lactic acidosis, and strokelike episodes: a distinctive clinical syndrome. Ann. Neurol. 16, 481–488.

Rusanen, H., Majamaa, K., Hassinen, I.E., 2000. Increased activities of antioxidant enzymes and decreased ATP concentration in cultured myoblasts with the 3243A–>G mutation in mitochondrial DNA. Biochim. Biophys. Acta 1500, 10–16.

Saeed, A.I., Sharov, V., White, J., Li, J., Liang, W., Bhagabati, N., Braisted, J., Klapa, M., Currier, T., Thiagarajan, M., Sturn, A., Snuffin, M., Rezantsev, A., Popov, D., Ryltsov, A., Kostukovich, E., Borisovsky, I., Liu, Z., Vinsavich, A., Trush, V., Quackenbush, J., 2003. TM4: a free, open-source system for microarray data management and analysis. Biotechniques 34, 374–378.

Saito, K., Kimura, N., Oda, N., Shimomura, H., Kumada, T., Miyajima, T., Murayama, K., Tanaka, M., Fujii, T., 2012. Pyruvate therapy for mitochondrial DNA depletion syndrome. Biochim. Biophys. Acta 1820, 632–636.

Sandhu, J.K., Sodja, C., McRae, K., Li, Y., Rippstein, P., Wei, Y.H., Lach, B., Lee, F., Bucurescu, S., Harper, M.E., Sikorska, M., 2005. Effects of nitric oxide donors on cybrids harbouring the mitochondrial myopathy, encephalopathy, lactic acidosis and stroke-like episodes (MELAS) A3243G mitochondrial DNA mutation. Biochem. J. 391, 191–202.

Scherz-Shouval, R., Shvets, E., Fass, E., Shorer, H., Gil, L., Elazar, Z., 2007. Reactive oxygen species are essential for autophagy and specifically regulate the activity of Atg4. EMBO J. 26, 1749–1760.

Soga, T., Ohashi, Y., Ueno, Y., Naraoka, H., Tomita, M., Nishioka, T., 2003. Quantitative metabolome analysis using capillary electrophoresis mass spectrometry. J. Proteome Res. 2, 488–494.

Soga, T., Baran, R., Suematsu, M., Ueno, Y., Ikeda, S., Sakurakawa, T., Kakazu, Y., Ishikawa, T., Robert, M., Nishioka, T., Tomita, M., 2006. Differential metabolomics reveals ophthalmic acid as an oxidative stress biomarker indicating hepatic glutathione consumption. J. Biol. Chem. 281, 16768–16776.

Soga, T., Ishikawa, T., Igarashi, S., Sugawara, K., Kakazu, Y., Tomita, M., 2007. Analysis of nucleotides by pressure-assisted capillary electrophoresis-mass spectrometry using silanol mask technique. J. Chromatogr. A 1159, 125–133.

Sproule, D.M., Kaufmann, P., 2008. Mitochondrial encephalopathy, lactic acidosis, and strokelike episodes: basic concepts, clinical phenotype, and therapeutic management of MELAS syndrome. Ann. N. Y. Acad. Sci. 1142, 133–158.

Sugimoto, M., Wong, D.T., Hirayama, A., Soga, T., Tomita, M., 2010. Capillary electrophoresis mass spectrometry-based saliva metabolomics identified oral, breast and pancreatic cancer-specific profiles. Metabolomics 6, 78–95.

Tanaka, M., Borgeld, H.J., Zhang, J., Muramatsu, S., Gong, J.S., Yoneda, M., Maruyama, W., Naoi, M., Ibi, T., Sahashi, K., Shamoto, M., Fuku, N., Kurata, M., Yamada, Y., Nishizawa, K., Akao, Y., Ohishi, N., Miyabayashi, S., Umemoto, H., Muramatsu, T., Furukawa, K., Kikuchi, A., Nakano, I., Ozawa, K., Yagi, K., 2002. Gene therapy for mitochondrial disease by delivering restriction endonuclease SmaI into mitochondria. J. Biomed. Sci. 9, 534–541.

Tanaka, M., Nishigaki, Y., Fuku, N., Ibi, T., Sahashi, K., Koga, Y., 2007. Therapeutic potential of pyruvate therapy for mitochondrial diseases. Mitochondrion 7, 399–401.

van Winden, W.A., Wittmann, C., Heinzle, E., Heijnen, J.J., 2002. Correcting mass isotopomer distributions for naturally occurring isotopes. Biotechnol. Bioeng. 80, 477–479.

Voet, D., Voet, J.G., 1995. Biochemistry, Second ed. John Wiley & Sons, New York.

Wilichowski, E., Korenke, G.C., Ruitenbeek, W., De Meirleir, L., Hagendorff, A., Janssen, A.J., Lissens, W., Hanefeld, F., 1998. Pyruvate dehydrogenase complex deficiency and altered respiratory chain function in a patient with Kearns-Sayre/MELAS overlap syndrome and A3243G mtDNA mutation. J. Neurol. Sci. 157, 206–213.

Yoneda, M., Tanaka, M., Nishikimi, M., Suzuki, H., Tanaka, K., Nishizawa, M., Atsumi, T., Ohama, E., Horai, S., Ikuta, F., Miyatake, T., Ozawa, T., 1989. Pleiotropic molecular defects in energy-transducing complexes in mitochondrial encephalomyopathy (MELAS). J. Neurol. Sci. 92, 143–158.

Yoneda, M., Miyatake, T., Attardi, G., 1994. Complementation of mutant and wild-type human mitochondrial DNAs coexisting since the mutation event and lack of complementation of DNAs introduced separately into a cell within distinct organelles. Mol. Cell. Biol. 14, 2699–2712.

Zhang, J., Yoneda, M., Naruse, K., Borgeld, H.J., Gong, J.S., Obata, S., Tanaka, M., Yagi, K., 1998. Peroxide production and apoptosis in cultured cells carrying mtDNA mutation causing encephalomyopathy. Biochem. Mol. Biol. Int. 46, 71–79.

Chromosome Res (2012) 20:659–672
DOI 10.1007/s10577-012-9300-5

Visualization of the spatial positioning of the *SNRPN*, *UBE3A*, and *GABRB3* genes in the normal human nucleus by three-color 3D fluorescence in situ hybridization

Rie Kawamura · Hideyuki Tanabe · Takahito Wada · Shinji Saitoh · Yoshimitsu Fukushima · Keiko Wakui

Received: 13 February 2012 / Revised: 14 June 2012 / Accepted: 14 June 2012 / Published online: 17 July 2012

Abstract The three-dimensional (3D) structure of the genome is organized non-randomly and plays a role in genomic function via epigenetic mechanisms in the eukaryotic nucleus. Here, we analyzed the spatial positioning of three target regions; the *SNRPN*, *UBE3A*, and *GABRB3* genes on human chromosome 15q11.2–q12, a representative cluster of imprinted regions, in the interphase nuclei of B lymphoblastoid cell lines, peripheral blood cells, and skin fibroblasts derived from normal individuals to look for evidence of genomic organization and function. The positions of these genes were simultaneously visualized, and all inter-gene distances were calculated for each homologous chromosome in each nucleus after three-color 3D fluorescence in situ hybridization. None of the target genes were arranged linearly in most cells analyzed, and *GABRB3* was positioned closer to *SNRPN* than *UBE3A* in a high proportion of cells in all cell types. This was in contrast to the genomic map in which *GABRB3* was positioned closer to *UBE3A* than *SNRPN*. We compared the distances from *SNRPN* to *UBE3A* (SU) and from *UBE3A* to *GABRB3* (UG) between alleles in each nucleus, 50 cells per subject. The results revealed that the gene-to-gene distance of one allele was longer than that of the other and that the SU ratio (longer/shorter SU distance between alleles) was larger than the UG ratio

Responsible Editor: Tatsuo Fukagawa

Electronic supplementary material The online version of this article (doi:10.1007/s10577-012-9300-5) contains supplementary material, which is available to authorized users.

R. Kawamura · T. Wada · Y. Fukushima · K. Wakui (✉)
Department of Medical Genetics,
Shinshu University School of Medicine,
3-1-1 Asahi,
Matsumoto, Nagano 390-8621, Japan
e-mail: kwakui@shinshu-u.ac.jp

H. Tanabe
Department of Evolutionary Studies of Biosystems,
School of Advanced Sciences,
The Graduate University for Advanced Studies (Sokendai),
Shonan Village,
Hayama, Kanagawa 240-0193, Japan

T. Wada
Division of Pediatric Neurology, Kanagawa Children's Medical Center,
2-138-4, Mutsukawa, Minami-ku,
Yokohama 232-8555, Japan

S. Saitoh
Department of Pediatrics and Neonatology, Nagoya City University Graduate School of Medical Sciences,
1 Kawasumi, Mizuho-cho, Mizuho-ku,
Nagoya 467-8601, Japan

(longer/shorter UG distance between alleles). The UG distance was relatively stable between alleles; in contrast, the SU distance of one allele was obviously longer than the distance indicated by the genome size. The results therefore indicate that *SNRPN*, *UBE3A*, and *GABRB3* have non-linear and non-random curved spatial positioning in the normal nucleus, with differences in the SU distance between alleles possibly representing epigenetic evidence of nuclear organization and gene expression.

Keywords Genome organization · Spatial positioning · 3D-FISH · *SNRPN* · Chromatin · Epigenetic

Abbreviations

3C	Chromosome conformation capture
3D	Three dimensional
4C	3C-on chip or circular 3C
AS	Angelman syndrome
BAC	Bacterial artificial chromosome
CT	Chromosome territory
FBs	Skin fibroblasts
FISH	Fluorescence in situ hybridization
FPC	Fluorescence peak center
GABRB3	Gamma-aminobutyric acid (GABA) A receptor, beta 3
IQR	Interquartile range
LCLs	B lymphoblastoid cell lines
PB	Peripheral blood
PWS	Prader–Willi syndrome
SNRPN	Small nuclear ribonucleoprotein polypeptide N
UBE3A	Ubiquitin-protein ligase E3A

Introduction

Recent experimental and computational advances have generated spatial information about nuclear architecture. We now know that the human genome, containing some 23,000 genes and 3.2 billion base pairs of DNA, is distributed among the 22 pairs of autosomes and two sex chromosomes, all of which are packed into the current chromatin compaction model. Interphase chromosomes are generally considered to be less condensed than their mitotic counterparts. To understand the complex workings of the genome in full, it is necessary to consider its three-dimensional (3D) organization, rather than relying on linear information alone (Laster and Kosak 2010; Joffe et al. 2010). According to recent studies, higher-order chromatin organization and the spatial arrangement of genomic regions within the nucleus seem to play an important role in genome function via epigenetic mechanisms (Sproul et al. 2005; Lanctôt et al. 2007; Fraser and Bickmore 2007; Takizawa et al. 2008; Solovei et al. 2009; Ferrai et al. 2010; Egecioglu and Brickner 2011). Such findings were obtained by microscopic and, more recently, non-microscopic approaches. Microscopic techniques, such as 3D fluorescence in situ hybridization (3D-FISH) analysis, which although limited in resolution, provide spatial information such as physical distance, shape, and localization at the single-cell level (Shopland et al. 2006, Cremer and Cremer 2010; Crutchley et al. 2010). In 3D-FISH, radial positions and gene-to-gene distance are analyzed by the hybridization of probes to 3D-preserved nuclei. 3D-FISH studies have shown that individual chromosomes occupy discrete compartments called chromosome territories (CTs) that do not overlap with each other while adopting a preferential radial position within the nucleus. In many cell types, the radial organization of CTs is dependent on gene density or chromosome size. For instance, in rather spherically shaped nuclei, such as in lymphocytes, gene-dense chromosomes are located more internally while gene-poor chromosomes are located more peripherally (Croft et al. 1999; Boyle et al. 2001; Cremer et al. 2001; Tanabe et al. 2002). Bolzer et al. (2005) were the first to use 24-color 3D-FISH to simultaneously detect all chromosomes in human fibroblasts of interphase nuclei, presenting 3D maps of all CTs. Some genes change their nuclear location depending on gene activity (Lanctôt et al. 2007; Meaburn et al. 2007; Solinhac et al. 2011). For example, some genes loop out from their CT when active (Volpi et al. 2000; Williams et al. 2002; Mahy et al. 2002; Chambeyron and Bickmore 2004; Küpper et al. 2007; Ferrai et al. 2010). In this way, various genome organization phenomena have been microscopically observed.

Non-microscopic studies, such as chromosome conformation capture (3C) and 3C-based analysis, including 3C-on chip or circular 3C (4C), 3C-carbon copy (5C), chromatin interaction analysis by paired-end tag sequencing (ChIA-PET), and Hi-C, which although requiring large numbers of cells, provide spatial information of physical contact between

chromatin segments at a high resolution (Dekker et al. 2002; Simonis et al. 2006; Zhao et al. 2006; Dostie et al. 2006; Fullwood et al. 2009; Lieberman-Aiden et al. 2009; Handoko et al. 2011). In particular, 3C-based methods make it possible to determine genome-wide chromatin interaction frequency. In the 3C method, the frequency of spatial contacts between genomic loci is analyzed using formaldehyde cross-linking, ligation, and locus-specific PCR (Dekker et al. 2002). Several 3C and 3C-based studies have suggested that long-range chromatin interactions are involved in the epigenetic regulation of gene expression (Simonis et al. 2007; de Wit and de Laat 2012). For instance, the higher-order chromatin conformation at some loci differs between maternal and paternal alleles, and is correlated with the formation of CCCTC-binding factor (zinc finger protein) (CTCF)-dependent parent-of-origin specific loops (Murrell et al. 2004). Long-range looping interactions between genes can occur over a genomic distance of a few kb to tens of Mb (Simonis et al. 2006; Lieberman-Aiden et al. 2009; van Steensel and Dekker 2010). Furthermore, chromatin contacts not only occur between specific short functional elements, such as enhancers and promoters, but also over larger chromosomal domains, such as intrachromosomal (*cis*), interchromosomal (*trans*), and genomic environment contacts, when active genes share a transcription factory (Crutchley et al. 2010; van Steensel and Dekker 2010). Consequently, it seems that chromatin communicates as a spatial network in interphase nuclei. Such approaches complement each other by offering new insight into genomic spatial organization and function in the nucleus (Dekker 2008; Cremer and Cremer 2010; Crutchley et al. 2010, de Wit and de Laat 2012).

Despite previous findings, information on the relationship between genomic organization and function remains limited. In an attempt to further investigate, we focused on the following three genes in imprinted loci on 15q11.2–q13: *SNRPN*, which exhibits monoallelic (paternal) expression; *UBE3A*, which exhibits tissue-specific (e.g., brain) maternal expression; and *GABRB3*, which exhibits biallelic expression. Human chromosome 15q11–q13, a region subjected to genomic imprinting, is responsible for Prader–Willi syndrome (PWS) and Angelman syndrome (AS) (Horsthemke and Wagstaff 2008). The lack of a functional paternal copy of 15q11–q13 causes PWS, while the lack of a functional maternal copy of *UBE3A* causes AS. Several groups have studied the spatial organization of 15q11–q13 using 3D image analysis. For example, Nogami et al. (2000) examined the relationship between *SNRPN* and chromosome territory in human myeloid leukemia HL60 cells. Teller et al. (2007) investigated the 3D distance between PWS/AS homologous regions in human lymphocytes, fibroblasts, and a gorilla lymphoblastoid cell line to examine the "chromosome kissing" hypothesis during the late S phase of interphase. Rauch et al. (2008) studied chromatin architecture within the PWS locus in a human lymphoblastoid cell line and fibroblast cell nuclei. They measured 3D distance between two of four probes located within 230 kb and analyzed chromatin compaction using computer simulations. However, they found no clearly detectable differences between the active and inactive PWS domains.

Although various observations have accumulated regarding the imprinted regions of PWS/AS, there are still insufficient data from a spatial viewpoint with regard to the relationship between higher-order chromatin configuration and gene activity. To the best of our knowledge, this is the first study to use three-color 3D-FISH to investigate spatial organization in the PWS/AS regions of three consecutive genomic regions—*SNRPN*, *UBE3A*, and *GABRB3*—in the nuclei of human B lymphoblastoid cell lines (LCLs), peripheral blood (PB) cells, and skin fibroblasts (FBs) derived from normal individuals.

In this study, we measured all 3D inter-gene distances between two of three target genes on each homologous chromosome in each cell to search for new evidence of genomic organization and function. As activity of the imprinted genes differs according to parental origin, simultaneous visualization of the genes by three-color 3D-FISH at the single-cell level was the only feasible approach, regardless of advances in 3C and 3C-based analyses. Here, we report both the regularity and differences in spatial organization among the three target regions in the nucleus. Our results provide possible epigenetic evidence of a relationship between gene-to-gene distance and genome function.

Materials and methods

Cell materials and preparation of specimens

Epstein–Barr virus-transformed human B LCLs, mononuclear cells isolated from whole heparinized

PB cells, and FBs from a healthy female individual with normal karyotype (F-LCL, F-PB, and F-FB), and LCLs and PB cells from a healthy male individual with normal karyotype (M-LCL and M-PB) were obtained for 3D-FISH analyses. Ethical approval for this project was granted by the Institutional Review Board of Shinshu University School of Medicine.

PB cells were isolated by Ficoll–Paque density gradient centrifugation, and red blood cells were removed using RBC Lysis Solution (Qiagen). PB cells were resuspended in saline at a concentration of approximately 1×10^7 cells/mL.

LCLs and FBs in culture were synchronized for collection of large cell populations at G1 phase by the double-thymidine block method according to the standard procedure (Harper 2005) with minor modifications to analyze under conditions similar to PB cells at G0 phase. The releasing time was decided according to the doubling time of each cell type. LCLs were maintained in 10 % fetal bovine serum (FBS)/Roswell Park Memorial Institute 1640 (RPMI) medium at 37 °C in an atmosphere of 5 % CO_2. Exponentially growing LCLs were blocked with excess thymidine (2 mM) for 12 h, and released for 12 h, then blocked again for 12 h, after that they were released for 15 h to synchronized G1 phase. LCLs were resuspended in 10 % FBS/RPMI at a concentration of approximately 1×10^7 cells/mL. Suspended PB cells and LCLs from each subject were incubated at 37 °C for 1 h on poly-L-lysine-coated glass coverslips (24×60 mm). FBs were grown on coverslips with 10 % FBS/Dulbecco's modified Eagle's medium at 37 °C in 5 % CO_2 and were blocked with 2 mM thymidine for 12 h, then released for 12 h, and blocked again at 12 h, after that they were released for 15–15.5 h. The percentages of the cell cycle phase fractions of G0/G1, S, and G2/M in cultured cells were analyzed using FACSCalibur and CellQuest Pro software (Becton Dickinson). More than 75 % G0/G1 cell populations of synchronized LCLs and FBs were used for 3D-FISH analyses.

All cell materials on coverslips were fixed and prepared to obtain 3D preserved cell nuclei according to the methods described previously (Cremer et al. 2001; Solovei et al. 2002) with slight modifications as follows. All coverslips with cells for 3D-FISH analysis were briefly washed with phosphate-buffered saline (PBS), fixed in 4 % paraformaldehyde (PFA) in 0.3×PBS for 10 min, and washed again in PBS. For permeabilization, cells were treated with 0.5 % saponin and 0.5 % Triton X-100 in PBS for 20 min, washed in PBS, and after incubation in 20 % glycerol in PBS for at least 30 min, subjected to repeated freeze–thaw cycles in liquid nitrogen five times. After washing cells again in PBS, they were incubated for 10 min in 0.1 N HCl, washed in PBS, incubated in 0.002 % pepsin in 0.01 N HCl at 37 °C for 2–6 min, and washed with 0.05 M $MgCl_2$ in PBS. Cells were postfixed with 1 % PFA in PBS for 10 min, washed in PBS, and then in 2× SSC for 5 min. Cells on coverslips were stored at 4 °C in 50 % formamide in 2× SSC until hybridization.

FISH probes

For measurement of gene-to-gene 3D distance in nuclei, we focused on one of the representative clusters in a human imprinting region that includes the *SNRPN*, *UBE3A*, and *GABRB3* genes mapped on 15q11.2–q12 within the region responsible for PWS and AS. *SNRPN* is a gene with paternal-only expression, *UBE3A* is the gene responsible for AS and shows maternal>paternal tissue-specific expression, and *GABRB3* is expressed from both parental alleles (Horsthemke and Wagstaff 2008).

Five human bacterial artificial chromosome (BAC) clones were selected by genome data base and purchased from BACPAC Resources at Children's Hospital and Research Center (Oakland) as three target regions of FISH probes. The probe S region including the *SNRPN* gene (RP11-98D02 and RP11-642G3), the probe U region including *UBE3A* (RP11-234J13), and the probe G region including *GABRB3* (RP11-48C8 and RP13-687N06) (Fig. 1a). Each BAC clone DNA was cultured and extracted using the standard alkaline lysis mini-prep protocol and tested for correct chromosomal location and the absence of signals on the pericentromeric region of one chromosome 15 homolog using metaphase spreads of LCLs from a PWS patient with a deletion of 15q11.2–q13 (PWS-del) by FISH. It was confirmed that the signal of each BAC clone was absent on one chromosome 15q homolog of the metaphase from PWS-del.

According to the primary structure of the human genome, the center of probe S to the center of probe U (SU region) is physically separated by about 451 kb, and the center of probe U to the center of probe G (UG region) is about 1,298 kb; thus SU region:UG region=0.35:1. If chromosome condensation occurs over the entire chromosome, this proportion must remain the same.

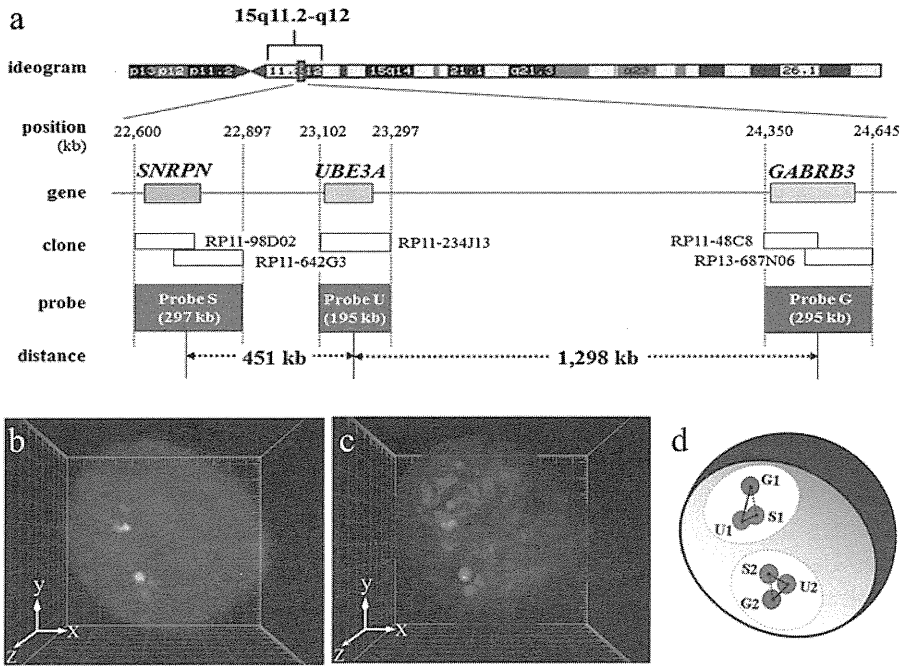

Fig. 1 **a** Probe design for three-color 3D-FISH analysis of the target region on human chromosome 15q11.2–q12. **b**, **c** Visualization of three-color 3D-FISH on structurally preserved human LCL nuclei and an image of 3D distance measurements. FISH with probes S (*green*), U (*red*), and G (*magenta*), showing the *SNRPN*, *UBE3A*, and *GABRB3* genes, respectively. Nuclei were counterstained with DAPI (*blue*). 3D reconstruction (**c**) was carried out from the captured image (**b**) obtained with Imaris software. Each signal spot was generated using the coordinate value from the FPC of each probe (i.e., probes S (*green*), U (*red*), and G (*magenta*)). Grid space, 1 μm. **d** Diagram of the relative 3D intergenic distance measurements. *Circles* colored *light yellow* represent the assumed chromosome territories 15. S1U1<S2U2 distance

Three-color 3D-FISH and probe detection

About 0.5 μg of DNA from each probe was used for each hybridization. Probe S, probe U, and probe G were labeled using a nick-translation kit (Abbott) with SpectrumGreen-dUTP, SpectrumOrange-dUTP (Abbott), and Cy5-dCTP (GE Healthcare), respectively, according to the manufacturer's protocol, to measure gene-to-gene distances on each homologous chromosome 15.

3D-FISH and probe detection were performed according to protocols described elsewhere (Cremer et al. 2001; Solovei et al. 2002) with slight modifications.

Labeled probe DNAs of three target regions and Cot-1 DNA were mixed and subjected to ethanol precipitation, and then resuspended in hybridization solution (50 % formamide and 10 % dextran sulfate in 2× SSC). The probes were predenatured at 80.5 °C for 6 min and placed on ice for 1 min. Denatured probes were applied to the coverslips on which fixed cells, covered with smaller coverslips (18×18 mm), and sealed. The coverslip specimens were denatured at 75 °C for 5 min, and hybridization was performed in a moist chamber at 37 °C for 3–4 days. The specimens were washed in 2× SSC, 0.1× SSC at 60 °C, 4× SSC with 0.2 % Tween 20, and 4× SSC. Nuclear DNA was counterstained with 4′,6-diamidino-2-phenylindole (DAPI) and the slides were mounted in Vectashield Antifade (Vector).

Confocal microscopic Image

Nuclei were scanned with a four-channel laser-scanning confocal microscope (Zeiss LSM5 EXCITER; Carl Zeiss MicroImaging GmbH) equipped with a Plan-Apochromat 63×/1.4 Oil DIC objective lens. For each optical section, images were collected sequentially for four fluorochromes (SpectrumGreen, SpectrumOrange, Cy5, and DAPI) using blue diode (405 nm), argon (488 nm), and helium-neon (543/633 nm) lasers, respectively.

To improve the signal-to-noise ratio, each sectional image obtained was an average of two successive scans. The focus *z*-step between sections was

0.364 μm. Stacks of 12-bit grayscale two-dimensional images were obtained with 512×140–320 pixels in each channel.

Confocal image stacks were processed with the microscope operating software (ZEN; Carl Zeiss MicroImaging GmbH) and saved as LSM files. More than 50 nuclear images were captured from each cell material. Nuclei from cultured cells with singlet-singlet signals were adopted for calculation as in G1 phase of the cell cycle but with doublet-doublet or singlet-doublet signals for each probe, which were suspected to be in S or G2 phase, were not selected for capture.

Quantitative 3D evaluation

We specified the 3D coordinates of three target regions at a time in each cell and calculated the actual measured value between two of the three regions, and then determined the spatial organization among these regions in the nucleus. Various 3D measurement data, such as the coordinate value of the fluorescence peak center (FPC) of each signal/nucleus volume/sphericity/ellipsoid axis length x, y, and z, were obtained using scientific 3D and 4D image processing and analysis software (Imaris, Imaris MeasurementPro, and ImarisCell; Bitplane).

Nuclei with sphericity of <0.5, suspected to be unable to maintain initially ordered 3D structures of the cells, were excluded from the calculation as the deformed nuclear shape leads to distortion of gene topology. Finally, 50 nuclei of each cell material were analyzed.

We measured the relative 3D gene-to-gene distance of three target regions, *SNRPN* (S), *UBE3A* (U), and *GABRB3* (G) genes at 15q11.2–q12 on each homologous chromosome 15 within the interphase nuclei, beginning with the 3D coordinate value of FPC of six fluorescent signals of the probes determined while checking 3D images of each nucleus simultaneously. We defined as "allele 1" on one of the homologous chromosomes 15 that had a shorter probe S-to-U distance (SU distance) than the other homologous chromosomes 15, and the FPC of probes S/U/G were defined as S1/U1/G1 on allele 1 in each nucleus. The FPC of probes S/U/G were defined as S2/U2/G2 on allele 2, which had a longer SU distance in each nucleus. Diagram of 3D distance measurements is shown in Fig. 1d. The shortest physical distances between two of the three probes—SU distance, UG distance, and SG distance—on each homologous chromosome 15 were calculated from the x, y, and z coordinates of the FPC of signals using the following equation and the spreadsheet application Excel (Microsoft Corporation).

$$\delta_{ij} = \sqrt{(x_i - x_j)^2 + (y_i - y_i)^2 + (z_i - z_i)^2}$$

*any two loci i and j

We also calculated angle U, which was defined as an internal angle formed by SU and UG sides, from the measurement data of distances SU, UG, and SG using the second cosine theorem with the following equation and the spreadsheet application Excel (Microsoft Corporation).

$$\theta = \cos^{-1}\frac{b^2+c^2-a^2}{2\times b\times c}$$

*θ: angle U, side b/c/a: distance SU/UG/SG

Statistical analysis

Fifty nuclei of each cell material were examined. We performed exploratory data analysis to find patterns in our results. Normality was assessed with the Shapiro–Wilk test. The distribution of measurements in a proportion of samples was not normal. Therefore, all measurements were analyzed using the nonparametric Mann–Whitney test between different cell types within the same individuals and between the same cell types among individuals. All statistical tests were two-sided, and $P<0.05$ was considered to indicate statistical significance. For multiple comparisons, significance levels were modified according to Bonferroni's correction (α). All statistical analyses were performed with SPSS software version 18.0 (IBM).

Results

Three-color 3D-FISH was performed to measure gene-to-gene distance on 15q11.2–q12, on each homologous part of chromosome 15, within each interphase nucleus from the three different cell types examined (Figs. 1 and 2). The 3D gene-to-gene distance, angle U from 100 alleles in 50 nuclei, and the radius, volume, and sphericity of 50 nuclei in each subject are summarized in Table 1. Values were corrected according to the average x-, y- and z-axis radius to enable comparisons of gene-to-gene distance between different subjects.

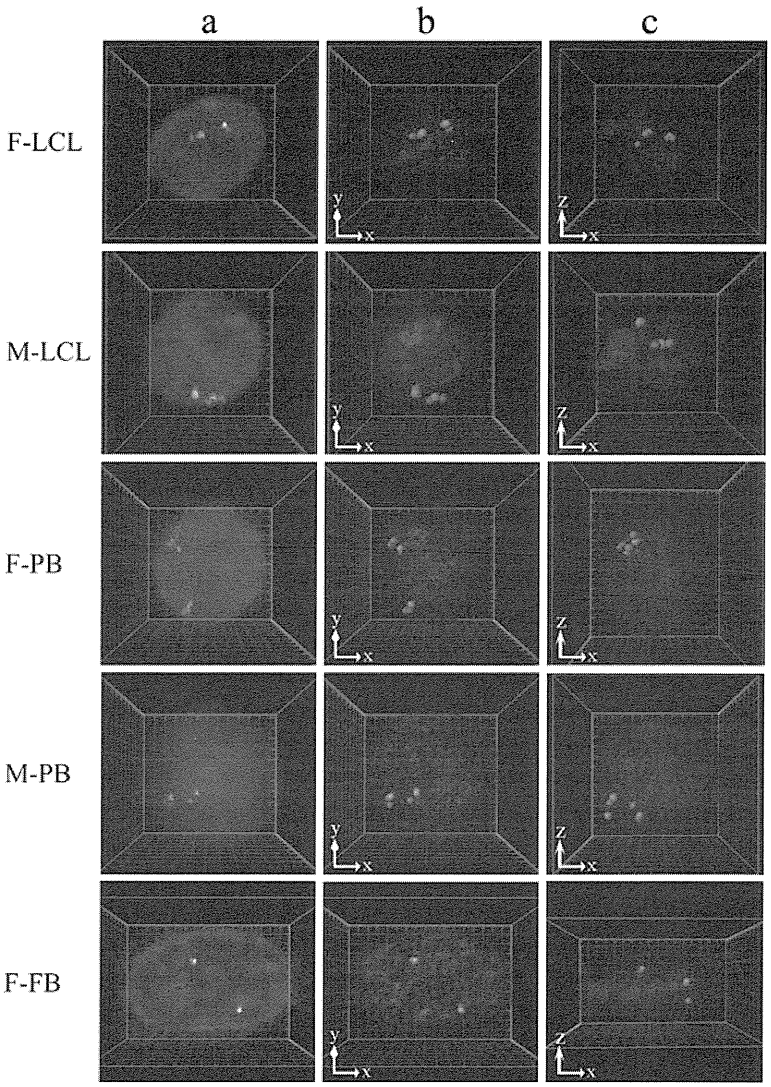

Fig. 2 Examples of three-color 3D-FISH results of projections and 3D reconstructions in typical nuclei from each subject. *Green/red/magenta* signals: probes S/U/G. 3D reconstructions in the *xy* (**b**) and *xz* direction (**c**) were obtained from the captured image (**a**) generated by Imaris software. Grid space, 1 μm

Gene-to-gene distance of the target regions and spatial positioning

A set of three signals for probes S, U, and G were readily distinguished on each allele in all cells. The interquartile range (IQR) and medians of the SU/UG/SG distance are shown in Table 1. Overall, the SG distance was shorter than the value obtained by summing the SU and UG distance.

As the volume of the nucleus varied between subjects, and since gene-to-gene distance is thought to be influenced by nuclear volume (as shown in Table 1), comparisons of distance were made after normalizing the average nuclear radius of the *x*-, *y*-, and *z*-axis in each subject (Fig. 3). The SU/UG/SG distance were significantly different between LCLs, PB cells, and FBs of the same individual ($P<0.0005$, UG and SG distances between F-LCLs and F-FBs; $P=0.004$, $P=0.007$, respectively; Bonferroni's correction, $\alpha<0.008$), except for the SU distance between F-LCLs and F-FBs. There was no significant difference between identical cell types from different individuals for LCLs and PB cells (F-LCLs and M-LCLs; F-PB and M-PB cells) (Fig. 3).

Angle U, defined as the internal angle formed by the SU and UG sides, also varied in size, with the median angle being approximately 60° in all subjects (Table 1; Fig. 3). There was no significant difference between different cell types of the same individual (F-LCLs, F-PB cells, and F-FBs; M-LCLs and M-PB

Table 1 3D distances of SU/UG/SG and angle U in the nucleus calculated using the 3D coordinate values of the FPC of probe signals and the radius, volume, and sphericity of the nucleus

Subjects	Measured value median (IQR; μm)			Measured value median (IQR)			
	Corrected value median[a] (IQR; %)						
	SU distance	UG distance	SG distance	Angle U[b] (degree)	Radius[c] (μm)	Volume (μm^3)	Sphericity
F-LCL	0.255 (0.170–0.366) 6.2 (4.0–8.6)	0.645 (0.436–0.864) 15.7 (10.4–20.6)	0.564 (0.352–0.771) 13.5 (8.2–18.3)	56 (34–73)	4.2 (4.0–4.3)	290 (264–318)	0.93 (0.91–0.94)
M-LCL	0.345 (0.248–0.523) 6.6 (4.8–10.0)	0.803 (0.571–1.000) 15.2 (11.2–19.1)	0.722 (0.504–0.898) 13.7 (9.5–17.6)	59 (41–86)	5.4 (5.2–5.5)	605 (531–637)	0.83 (0.77–0.88)
F-PB	0.439 (0.268–0.719) 8.3 (5.4–13.8)	0.945 (0.726–1.285) 18.7 (14.2–25.8)	0.895 (0.677—1.243) 17.7 (13.3–25.0)	59 (37–85)	5.0 (4.7–5.3)	515 (430–597)	0.93 (0.87–0.94)
M-PB	0.569 (0.326–1.068) 10.8 (6.7–18.6)	1.046 (0.759–1.434) 21.1 (15.0–26.6)	0.964 (0.68–1.324) 19.4 (13.7–26.0)	63 (34–88)	5.2 (4.5–5.7)	560 (372–710)	0.91 (0.88–0.94)
F-FB	0.423 (0.271–0.556) 6.6 (4.3–9.0)	0.806 (0.593–1.057) 12 (9.5–15.9)	0.674 (0.470–0.900) 9.9 (7.5–14.3)	53 (31–84)	6.1 (5.6–7.4)	683 (565–1152)	0.70 (0.65–0.75)

n=100 alleles, 50 nuclei from each subject

IQR interquartile range

[a] Median of corrected value by the radius (relative radius (in percent)). Measured value/radius × 100

[b] Internal angle formed by SU and UG sides

[c] Average of x-, y-, and z-axis radius

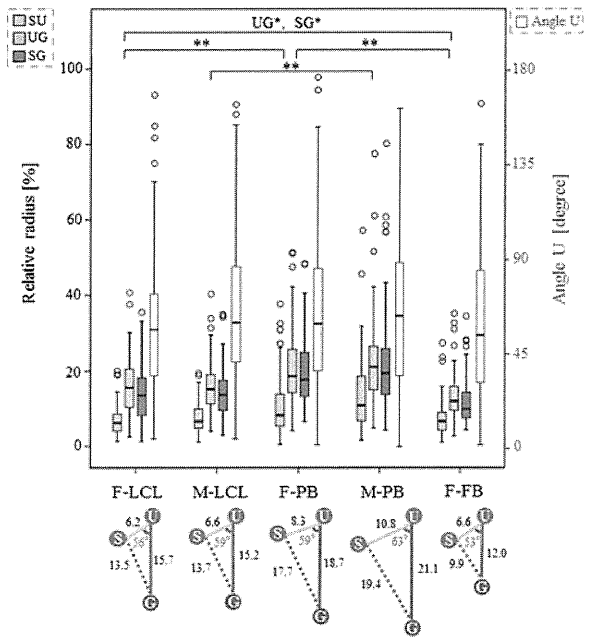

Fig. 3 Gene-to-gene distance of SU/UG/SG and angle U for each subject. The *colored boxes* and *whisker plots* show the distributions of SU, UG, and SG gene distance (corrected value, relative radius), and the *red-lined boxes* and *whisker plots* show the distributions of angle U. Angle U is defined as the internal angle formed by the SU and UG sides. The *left* axis in the graph shows the relative radius and the *right* axis the angle U. The *box plots* summarize data obtained using the median, upper, and lower quartiles, as well as the range. *Boxes* represent the 25th to 75th percentiles (IQR). The *solid line* within the boxes indicates the median. *Lower* and *upper whiskers* show the 10th and 90th percentiles, respectively, of the distribution. *Open circles* indicate outliers. For the SU/UG/SG distance and the angle U, *P* values were obtained using the Mann–Whitney test between different cell types of the same individuals (F-LCL, F-PB, and F-FB; M-LCL and M-PB) and between identical cell types from different individuals (F-LCL and M-LCL; F-PB and M-PB). A *P* value<0.008 was considered statistically significant after correcting for multiple comparisons (Bonferroni's correction, $\alpha=0.05/6=0.008$; $*P<0.008$; $**P<0.001$; $n=100$ alleles, 50 nuclei) The *bottom diagram* presents the summarized configuration of *SNRPN*, *UBE3A*, and *GABRB3* genes in the nucleus for each subject, cited according to the corrected median value of the SU/UG/SG distance and the angle U (Table 1)

cells), and between identical cell types from different individuals (F-LCLs and M-LCLs; F-PB and M-PB cells).

Distance ratio between alleles and between regions

We analyzed the 3D intergenic distance of three target genes between each homologous part of chromosome 15 for each allele in all subjects (Fig. 1d) to determine differences between alleles of each target region (e.g., S1U1 vs. S2U2) (Fig. 4a) and between adjacent parts of the same chromosome (e.g., S1U1 vs. U1G1) (Fig. 4b) within 3D nuclei. The median distance of S1U1, S2U2, U1G1, and U2G2 is shown in Table 2.

The distance ratio was defined as:

SU ratio=longer SU/shorter SU distance
UG ratio=longer UG/shorter UG distance

In all subjects, the median SU ratio was higher than the median UG ratio. The differences between the SU and UG ratios were significant in F-PBs and M-PB cells ($P=0.0004$ and $P=0.0037$, respectively; Bonferroni's correction, $\alpha<0.0045$). There was no significant difference in the SU and UG ratio between different cell types of the same individual (F-LCLs, F-PB cells, and F-FBs; M-LCLs and M-PB cells) and between identical cell types from different individuals (F-LCLs and M-LCLs; F-PB and M-PB cells) (Fig. 4a).

According to the genomic coordinates, SU is 451 kb and UG is 1,298 kb, therefore SU:UG=0.35:1. The median distance ratios were: S1U1/U1G1=0.32, S2U2/U2G2=0.48 in F-LCLs; S1U1/U1G=0.35, S2U2/U2G2=0.61 in M-LCLs; S1U1/U1G=0.28, S2U2/U2G2=0.58 in F-PB cells; S1U1/U1G=0.34, S2U2/U2G2=0.82 in M-PB cells; and S1U1/U1G1=0.41, S2U2/U2G2=0.75 in F-FBs (Fig. 4b, c). There was no significant difference in allele 1 between different cell types of the same individual (F-LCLs, F-PB cells, and F-FBs; M-LCLs and M-PB cells) and between identical cell types from different individuals (F-LCLs and M-LCLs; F-PB and M-PB cells). Similarly, there was no significant difference in allele 2 (Fig. 4b).

Discussion

The 3D structure of the genome is organized non-randomly and plays a role in genome function via epigenetic mechanisms in the human nucleus. However, the genome is far more complex than can be explained by linear information alone. The present study was therefore performed to investigate how consecutive genes including imprinting genes are arranged spatially in human interphase nuclei with the aim of acquiring knowledge of genomic organization and function. We focused on *SNRPN*, showing paternal expression only, and contiguous *UBE3A* and *GABRB3* genes and examined whether specific higher-order chromatin

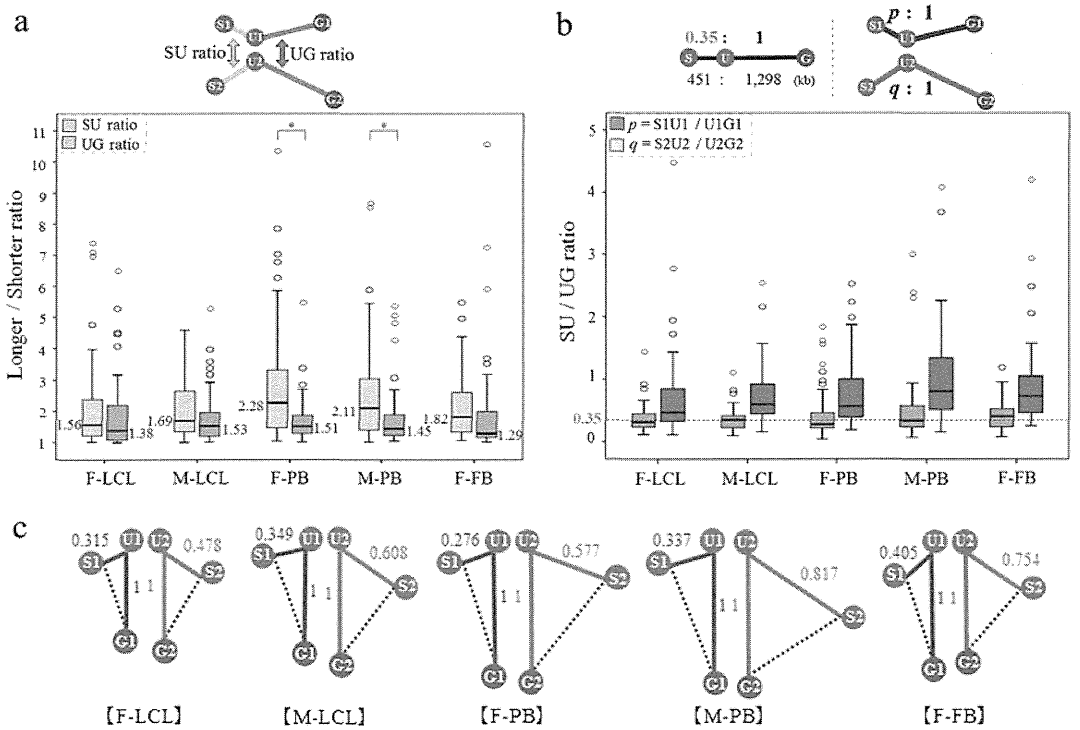

Fig. 4 Distance ratios between alleles and between regions. **a** SU and UG distance ratios between alleles in each cell for each subject. *Box* and *whisker* plots show the distributions of the distance ratio for each subject. Distance ratios were calculated as follows: SU ratio (*yellow lines* in the top diagram)=longer SU/shorter SU distance; UG ratio (*gray lines* in the top diagram)=longer UG/shorter UG distance. For both the SU and UG ratios, *P* values were obtained using the Mann–Whitney test within each subject and between subjects (F-LCL, F-PB, and F-FB; M-LCL and M-PB; F-LCL and M-LCL; and F-PB and M-PB). A *P* value<0.0045 was considered statistically significant after correcting for multiple comparisons (Bonferroni's correction, $\alpha=0.05/11=0.0045$; $*P<0.004$; $n=50$ nuclei). **b** SU/UG distance ratios of each allele for each subject. In the primary sequence of the human genome, SU:UG=451 kb:1,298 kb= 0.35:1 (*upper left diagram*). Ratio of the distance of S1U1when the distance of U1G1 was set to 1 (*blue lines* in the upper right diagram): *p*=S1U1/U1G1 (*blue box* and *whisker plots* in the graph). Ratio of the distance of S2U2 when the distance of U2G2 was set to 1 (*red lines* in the upper right diagram): *q*= S2U2/U2G2 (*red box* and *whisker plots* in the graph). The *dashed line* in the plot shows 0.35. For *p* and *q*, *P* values were obtained using the Mann–Whitney test between different cell types of the same individual (F-LCL, F-PB, and F-FB; M-LCL and M-PB) and between identical cell types from different individuals (F-LCL and M-LCL; F-PB and M-PB). A *P* value<0.0045 was considered statistically significant after correcting for multiple comparisons (Bonferroni's correction, $\alpha=0.05/6=0.008$); no significant difference was observed ($n=50$ nuclei). **c** Configuration of *SNRPN*, *UBE3A*, and *GABRB3* genes on homologous chromosomes in the nucleus for each subject drawn based on Table 2 and (**b**). Decimal fractions in *blue* indicate the median distance ratio of *p* as shown in (**b**). Likewise, decimal fractions in red denote the median distance ratio of *q*. The blue value "1" and red value "1" are not equal distances

organization could be observed microscopically using three-color 3D-FISH analysis in normal LCLs, PB cells, and FBs, all of which are used frequently for research (Figs. 1 and 2). Next, we evaluated regularity and differences in their spatial positioning (Figs. 3 and 4).

Gene-to-gene distances and spatial positioning of the target regions

We found that the *SNRPN*, *UBE3A*, and *GABRB3* genes had non-linear and non-random curved spatial organization in the human nucleus (Fig. 3). Microscopic observations indicated that a distance of about 500 kb was measurable for comparison between homologous parts on the chromatin. Rauch et al. (2008) found no clearly detectable differences between the active and inactive PWS domains, as measured by 3D distance between two of four probes located within 230 kb. Our results indicated that *GABRB3* tended to be located closer to *SNRPN* than *UBE3A*, in contrast to the genomic map. Moreover, the median values of the internal angle U were calculated as 53–63° (Fig. 3).

Table 2 Relative 3D distances of SU/UG/SG for each allele in the nucleus

Subjects	S1U1 distance (μm) Median (IQR)	U1G1 distance (μm) Median (IQR)	S1G1 distance (μm) Median (IQR)	S2U2 distance (μm) Median (IQR)	U2G2 distance (μm) Median (IQR)	S2G2 distance (μm) Median (IQR)
F-LCL	0.194 (0.124–0.273)	0.615 (0.429–0.765)	0.555 (0.360–0.740)	0.353 (0.251–0.448)	0.711 (0.440–0.933)	0.582 (0.350–0.893)
M-LCL	0.270 (0.166–0.334)	0.770 (0.597–0.936)	0.750 (0.638–0.878)	0.510 (0.356–0.601)	0.834 (0.547–1.038)	0.681 (0.433–0.901)
F-PB	0.273 (0.189–0.431)	0.908 (0.689–1.206)	0.856 (0.673–1.123)	0.652 (0.442–0.994)	0.987 (0.732–1.541)	0.968 (0.680–1.320)
M-PB	0.365 (0.228–0.594)	1.081 (0.756–1.424)	1.030 (0.754–1.319)	0.934 (0.549–1.187)	1.020 (0.781–1.437)	0.910 (0.581–1.331)
F-FB	0.271 (0.206–0.432)	0.852 (0.591–1.086)	0.692 (0.499–1.014)	0.531 (0.409–0.725)	0.803 (0.604–0.988)	0.657 (0.451–0.818)

n=50 nuclei from each subject

IQR interquartile range

4C analysis of human neuronal cells revealed that a PWS-imprinting center forms chromatin loops that contain key neurodevelopmental genes, including *GABRB3* (Yasui et al. 2011). Our results showing non-linear and non-random curved spatial organization of this region may support these findings.

Distance ratios between alleles and regions

We also found that gene-to-gene distance was not similar in size between alleles and regions (Fig. 4). The UG distance tended to be stable between alleles compared with the SU distance, even though the physical distance of UG is longer than that of SU according to the primary structure (Table 2). Figure 4a shows the differences in the SU and UG distance ratio between alleles; the SU ratio was larger than the UG ratio in all subjects. Comparison of the distance ratios between regions on the same allele revealed that the ratios of S2U2/U2G2 were >0.35, although those of S1U1/U1G1 were around 0.35 in all subjects (Fig. 4b). These results suggest that the S2U2 region may loosen more than the other region. It is generally believed that actively transcribed genes or genes poised for transcription are present in decondensed "open" chromatin configurations, while permanently silent genes are located within compact "closed" chromatin (Cremer et al. 2006). Regarding the PWS/AS region, Ohta et al. (1999) demonstrated that *SNRPN* chromatin is found in an open configuration exclusively on the paternal-derived allele. Thus, to summarize, the above results suggest that the degree of condensation seems to differ between homologous regions and adjacent regions of SU and UG.

Cell type specificity

The findings revealed that the spatial organization of the three target regions had a similar basic distribution in each of the three cell types examined. There were, however, subtle variations in gene-to-gene distance, which were dependent on cell type, even when from the same individual (Figs. 3 and 4). The *SNRPN* gene showed the same methylation pattern in a variety of tissues including LCLs, PB cells, and FBs (Glenn et al. 1996; Birney et al. 2010). Differences between cell types were related to the fact that PB cells and LCLs are in suspension, while FBs are adherent cells. The differences between PB cells and cultured cells were thought to be have been influenced by the cell cycle

since the PB cells were all in the G0 phase while the LCLs and FBs included G1, S, G2, and M phase cells, although the cultured cells were synchronized so the majority of the cell population was in the G1 phase. In addition, PB cells are composed of several kinds of mononuclear cells, in particular, T lymphocytes, B lymphocytes, and monocytes.

In this analysis, we examined 50 cells in each subject, and the obtained values of inter-gene distance displayed large variability among not only cycling cultured cells but also PB cells. Each fixed cell nucleus evaluated in the 3D-FISH analysis seemed to represent a snapshot in time of the higher-order structure and dynamics of chromatin (Teller et al. 2007; Cremer and Cremer 2010). Some investigations have shown that the movement of chromosomes and gene loci increases during early G1 (Walter et al. 2003) while other observations focusing on short-range chromatin motion suggest that local diffusional motion of chromatin is important in gene regulation (Soutoglou and Misteli. 2007). The probabilistic positioning of chromosomes can therefore show relatively large variation when single cells are compared. Furthermore, the 3D distance between genes in the nucleus is potentially influenced by chromatin compaction. Our results from the PB cells suggest that there is a range of chromatin compaction in the nucleus. Nishino et al. (2012) reported that human mitotic chromosomes consist predominantly of irregularly arranged nucleosome fibers, which they suggested exist in a similar state in the majority of active interphase nuclei. Our results will therefore help clarify chromatin structure in future studies.

3D-FISH using the three- or more-color approach is a powerful experimental tool for simultaneously visualizing the spatial positioning of multiple regions and comparing alleles in individual cells. However, it is also necessary to take into consideration the possible effects of the complicated process used to fix the cells and maintain their 3D structure for FISH analysis. It is difficult to preserve perfectly the 3D structure of nuclei from cells in suspension culture. Indeed, in this study, the volume of some nuclei could not be reproduced (data not shown).

In conclusion, the results of this study suggest that the *SNRPN*, *UBE3A*, and *GABRB3* loci have non-linear and non-random curved spatial organization in the nuclei of normal human cells. A distance of about 500 kb was measured microscopically for comparisons between homologous parts of chromatin within the nucleus. In addition, the differences in SU distance between alleles and between regions on each chromosome 15 seem to represent new epigenetic evidence of nuclear organization and gene expression. Confirmation of the relationship between activity and the 3D distance of imprinted genes in the nucleus now remains in future studies.

If the epigenetic hypothesis is confirmed whereby intergenic distance is shown to vary depending on gene activity, it could lead to further research on the development of new diagnostic techniques for patients in whom mutations cannot be identified. This would be a breakthrough in our understanding of the pathological processes of certain diseases with unknown causes, as well as adding to basic research on chromatin structure, of which much remains unknown.

Acknowledgments We acknowledge the support of Research Center for Human and Environmental Sciences, Shinshu University, and Department of Laboratory Medicine, Shinshu University Hospital. We would also like to thank Dr. Yoshiharu Yokokawa (Shinshu University School of Health Sciences) for his helpful suggestion about statistical analysis. This work was supported by Grant-in-Aid for challenging Exploratory Research (24659156 to K.W.), Grant-in-Aid for Scientific Research (C) (18590311 and 20590328 to K.W., and 19590331 to T.W.) from Japan Society for the Promotion of Science, Grant-in-Aid for Scientific Research (21602002 and 23125505 to H.T.) from the Ministry of Education, Culture, Sports, Science and Technology of Japan, Grant for Research Projects from Hayama Center for Advanced Studies (to H.T.) support in part by the Center for the Promotion of Integrated Sciences (CPIS) of Sokendai (to H.T.), and for Intractable Disorder Conquest Research Grant from Ministry of Health, Labor and Welfare of Japan (to T.W. and to Y.F.).

References

Birney E, Lieb JD, Furey TS, Crawford GE, Iyer VR (2010) Allele-specific and heritable chromatin signatures in humans. Hum Mol Genet 19:R204–R209

Bolzer A, Kreth G, Solovei I et al (2005) Three-dimensional maps of all chromosomes in human male fibroblast nuclei and prometaphase rosettes. PLoS Biol 3:e157

Boyle S, Gilchrist S, Bridger JM et al (2001) The spatial organization of human chromosomes within the nuclei of normal and emerin-mutant cells. Hum Mol Genet 10:211–219

Chambeyron S, Bickmore WA (2004) Chromatin decondensation and nuclear reorganization of the HoxB locus upon induction of transcription. Genes Dev 18:1119–1130

Cremer M, von Hase J, Volm T et al (2001) Non-random radial higher-order chromatin arrangements in nuclei of diploid human cells. Chromosom Res 9:541–567

Cremer T, Cremer M, Dietzel S et al (2006) Chromosome territories—a functional nuclear landscape. Curr Opin Cell Biol 18:307–316

Cremer T, Cremer M (2010) Chromosome territories. Cold Spring Harbor Perspect Biol 2:a003889

Croft JA, Bridger JM, Boyle S et al (1999) Differences in the localization and morphology of chromosomes in the human nucleus. J Cell Biol 145:1119–1131

Crutchley JL, Wang XQ, Ferraiuolo MA, Dostie J (2010) Chromatin conformation signatures: ideal human disease biomarkers? Biomark Med 4:611–629

Dekker J, Rippe K, Dekker M, Kleckner N (2002) Capturing chromosome conformation. Science 295:1306–1311

Dekker J (2008) Gene regulation in the third dimension. Science 319:1793–1794

de Wit E, de Laat W (2012) A decade of 3C technologies: insights into nuclear organization. Genes Dev 26:11–24

Dostie J, Richmond TA, Arnaout RA et al (2006) Chromosome conformation capture carbon copy (5C): a massively parallel solution for mapping interactions between genomic elements. Genome Res 16:1299–1309

Egecioglu D, Brickner JH (2011) Gene positioning and expression. Curr Opin Cell Biol 23:338–345

Ferrai C, de Castro IJ, Lavitas L, Chotalia M, Pombo A (2010) Gene positioning. Cold Spring Harb Perspect Biol 2: a000588

Fraser P, Bickmore W (2007) Nuclear organization of the genome and the potential for gene regulation. Nature 447:413–417

Fullwood MJ, Liu MH, Pan YF et al (2009) An oestrogen-receptor-alpha-bound human chromatin interactome. Nature 462:58–64

Glenn CC, Saitoh S, Jong MTC et al (1996) Gene structure, DNA methylation, and imprinted expression of the human *SNRPN* gene. Am J Hum Genet 58:335–346

Handoko L, Xu H, Li G et al (2011) CTCF-mediated functional chromatin interactome in pluripotent cells. Nat Genet 43:630–638

Harper JV (2005) Synchronization of cell populations in G1/S and G2/M phases of the cell cycle. Methods Mol Biol 296:157–166

Horsthemke B, Wagstaff J (2008) Mechanisms of imprinting of the Prader–Willi/Angelman region. Am J Med Genet A 146A:2041–2052

Joffe B, Leonhardt H, Solovei I (2010) Differentiation and large scale spatial organization of the genome. Curr Opin Genet Dev 20:562–569

Küpper K, Kölbl A, Biener D et al (2007) Radial chromatin positioning is shaped by local gene density, not by gene expression. Chromosoma 116:285–306

Lanctôt C, Cheutin T, Cremer M, Cavalli G, Cremer T (2007) Dynamic genome architecture in the nuclear space: regulation of gene expression in three dimensions. Nat Rev Genet 8:104–115

Laster K, Kosak ST (2010) Genomic Pangea: coordinate gene regulation and cell-specific chromosomal topologies. Curr Opin Cell Biol 22:314–319

Lieberman-Aiden E, van Berkum NL, Williams L et al (2009) Comprehensive mapping of long-range interactions reveals folding principles of the human genome. Science 326:289–293

Mahy NL, Perry PE, Bickmore WA (2002) Gene density and transcription influence the localization of chromatin outside of chromosome territories detectable by FISH. J Cell Biol 159:753–763

Meaburn KJ, Misteli T, Soutoglou E (2007) Spatial genome organization in the formation of chromosomal translocations. Semin Cancer Biol 17:80–90

Murrell A, Heeson S, Reik W (2004) Interaction between differentially methylated regions partitions the imprinted genes Igf2 and H19 into parent-specific chromatin loops. Nat Genet 36:889–893

Nishino Y, Eltsov M, Joti Y et al (2012) Human mitotic chromosomes consist predominantly of irregularly folded nucleosome fibres without a 30-nm chromatin structure. EMBO J 31:1644–1653

Nogami M, Kohda A, Taguchi H et al (2000) Relative locations of the centromere and imprinted *SNRPN* gene within chromosome 15 territories during the cell cycle in HL60 cells. J Cell Sci 113:2157–2165

Ohta T, Gray TA, Rogan PK et al (1999) Imprinting-mutation mechanisms in Prader–Willi syndrome. Am J Hum Genet 64:397–413

Rauch J, Knoch TA, Solovei I et al (2008) Light optical precision measurements of the active and inactive Prader–Willi syndrome imprinted regions in human cell nuclei. Differentiation 76:66–82

Shopland LS, Lynch CR, Peterson KA et al (2006) Folding and organization of a contiguous chromosome region according to the gene distribution pattern in primary genomic sequence. J Cell Biol 174:27–38

Simonis M, Klous P, Splinter E et al (2006) Nuclear organization of active and inactive chromatin domains uncovered by chromosome conformation capture-on-chip (4C). Nat Genet 38:1348–1354

Simonis M, Kooren J, de Laat W (2007) An evaluation of 3C-based methods to capture DNA interactions. Nat Methods 4:895–901

Solinhac R, Mompart F, Martin P et al (2011) Transcriptomic and nuclear architecture of immune cells after LPS activation. Chromosoma 120:501–520

Solovei I, Walter J, Cremer M et al (2002) FISH on three-dimensionally preserved nuclei. In: Squire J, Beatty B, Mai S (eds) FISH: a practical approach. Oxford University Press, Oxford, pp 119–157

Solovei I, Kreysing M, Lanctot C et al (2009) Nuclear architecture of rod photoreceptor cells adapts to vision in mammalian evolution. Cell 137:356–368

Soutoglou E, Misteli T (2007) Mobility and immobility of chromatin in transcription and genome stability. Curr Opin Genet Dev 17:435–442

Sproul D, Gilbert N, Bickmore WA (2005) The role of chromatin structure in regulating the expression of clustered genes. Nat Rev Genet 6:775–781

Takizawa T, Gudla PR, Guo L, Lockett S, Misteli T (2008) Allele-specific nuclear positioning of the monoallelically expressed astrocyte marker GFAP. Genes Dev 22:489–498

Tanabe H, Müller S, Neusser M et al (2002) Evolutionary conservation of chromosome territory arrangements in cell

nuclei from higher primates. Proc Natl Acad Sci U S A 99:4424–4429

Teller K, Solovei I, Buiting K, Horsthemke B, Cremer T (2007) Maintenance of imprinting and nuclear architecture in cycling cells. Proc Natl Acad Sci U S A 104:14970–14975

van Steensel B, Dekker J (2010) Genomics tools for unraveling chromosome architecture. Nat Biotechnol 28:1089–1095

Volpi EV, Chevret E, Jones T et al (2000) Large-scale chromatin organization of the major histocompatibility complex and other regions of human chromosome 6 and its response to interferon in interphase nuclei. J Cell Sci 113:1565–1576

Walter J, Schermelleh L, Cremer M, Tashiro S, Cremer T (2003) Chromosome order in HeLa cells changes during mitosis and early G1, but is stably maintained during subsequent interphase stages. J Cell Biol 160:685–697

Williams RR, Broad S, Sheer D, Ragoussis J (2002) Subchromosomal positioning of the epidermal differentiation complex (EDC) in keratinocyte and lymphoblast interphase nuclei. Exp Cell Res 272:163–175

Yasui DH, Scoles HA, Horike S et al (2011) 15q11.2-13.3 chromatin analysis reveals epigenetic regulation of CHRNA7 with deficiencies in Rett and autism brain. Hum Mol Genet 20:4311–4323

Zhao Z, Tavoosidana G, Sjölinder M et al (2006) Circular chromosome conformation capture (4C) uncovers extensive networks of epigenetically regulated intra- and interchromosomal interactions. Nat Genet 38:1341–1347

Neurogenetics (2012) 13:327–332
DOI 10.1007/s10048-012-0337-6

SHORT COMMUNICATION

A *DYNC1H1* mutation causes a dominant spinal muscular atrophy with lower extremity predominance

Yoshinori Tsurusaki · Shinji Saitoh · Kazuhiro Tomizawa · Akira Sudo · Naoko Asahina · Hideaki Shiraishi · Jun-ichi Ito · Hajime Tanaka · Hiroshi Doi · Hirotomo Saitsu · Noriko Miyake · Naomichi Matsumoto

Received: 24 February 2012 / Accepted: 3 July 2012 / Published online: 31 July 2012

Abstract Whole-exome sequencing of two affected sibs and their mother who showed a unique quadriceps-dominant form of neurogenic muscular atrophy disclosed a heterozygous *DYNC1H1* mutation [p.H306R (c.917A>G)]. The identical mutation was recently reported in a pedigree with the axonal form of Charcot–Marie–Tooth disease. Three other missense mutations in *DYNC1H1* were also identified in families with dominant spinal muscular atrophy with lower extremity predominance. Their clinical features were consistent with those of our family. Our study has demonstrated that the same *DYNC1H1* mutation could cause spinal muscular atrophy as well as distal neuropathy, indicating pleotropic effects of the mutation.

Keywords Spinal muscular atrophy with lower extremity predominance · DYNC1H1 · Whole-exome sequencing · Charcot–Marie–Tooth disease · Allelic disease

Introduction

DYNC1H1 encodes cytoplasmic dynein heavy chain 1, which is a subunit of the primary motor protein responsible for retrograde axonal transport in neurons [1]. Weedon et al. first identified a missense mutation [p.H306R (c.917A>G)] of *DYNC1H1* in a large family with axonal Charcot–Marie–Tooth (CMT) disease by using exome sequencing, indicating the significance of *DYNC1H1* in the peripheral nerve axon [2]. Subsequently, Harms et al. reported three other missense mutations in the tail domain of *DYNC1H1* in families with dominant spinal muscular atrophy with lower extremity predominance (SMA-LED, OMIM 158600), expanding the role of *DYNC1H1* to maintenance of motor neuron itself [3]. Recently, two de novo missense mutations have also been identified in patients with severe intellectual disability and variable neuronal migration defects [4].

Authorship Y.T. and S.S. contributed equally to this work.

Y. Tsurusaki · H. Doi · H. Saitsu · N. Miyake · N. Matsumoto (✉)
Department of Human Genetics, Yokohama City University Graduate School of Medicine,
3-9 Fukuura, Kanazawa-ku,
Yokohama 236-0004, Japan
e-mail: naomat@yokohama-cu.ac.jp

S. Saitoh (✉)
Department of Pediatrics and Neonatology, Graduate School of Medical Sciences, Nagoya City University,
Kawasumi-1, Mizuho-cho, Mizuho-ku,
Nagoya 467-8601, Japan
e-mail: ss11@med.nagoya-cu.ac.jp

K. Tomizawa
Department of Pediatrics, Nakashibetsu Town Hospital,
Nakashibetsu, Japan

A. Sudo
Department of Pediatrics, Sapporo City General Hospital,
Sapporo, Japan

N. Asahina · H. Shiraishi
Department of Pediatrics, Hokkaido University Graduate School of Medicine,
Sapporo, Japan

J.-i. Ito
Department of Pediatrics, Taiyo no Sono,
Date, Japan

H. Tanaka
Department of Pediatrics, Asahikawa Habilitation Center for Disabled Children,
Asahikawa, Japan

Therefore, *DNYC1H1* may have broad biological effects on development and maintenance of the nervous system.

In this study, we describe a family containing three individuals with dominant spinal muscular atrophy with lower extremity predominance. Exome sequencing identified an identical *DYNC1H1* mutation found in a pedigree with axonal CMT [2], demonstrating the pleotropic effects of the *DYNC1H1* mutation.

Subjects and methods

Subjects

Patient 1 This female patient was born after 41 weeks of gestation. Pregnancy was uneventful. Birth weight was 3,080 g. Her initial development was normal, and head control was recognized at 3–4 months. Late infantile motor development was mildly delayed, and she could walk unassisted at 1 year and 8 months. Unstable gait persisted thereafter, and she was referred to us at 3 years and 1 month of age for evaluation. On examination, proximal lower limb-dominant muscle atrophy and decreased deep tendon reflex were noted. Gower's sign was positive. No other neurological deficits were demonstrated. No sensory disturbance or ataxia was present.

The following examinations were performed at 3 years and 1 month of age. Neither serum transaminase nor creatine kinase was elevated. Motor nerve conduction velocity was within the normal limits (55.8 m/s for the right tibial nerve). Brain MRI revealed normal findings. Muscle computed tomography (CT) demonstrated severe atrophy and lipid degeneration, predominantly in the bilateral quadriceps femoris muscle (Fig. 1). The upper limbs and distal lower limbs were not affected. A muscle biopsy from the quadriceps femoris muscle demonstrated severe grouping atrophy of type 2 fibers with a massive increase in the amount of fibrous tissue and sparse enlarged type 1 fibers (Fig. 2).

The patient is currently 18 years old and graduated from regular high school. Her motor development has steadily progressed, and she only shows moderate proximal lower limb-dominant muscle weakness and atrophy. She can walk unassisted and shows a waddling gait and positive Gower's sign. No sensory disturbance or ataxia is noted. She does not have any intellectual disability.

Patient 2 Patient 2 is the half brother of patient 1. He was born after 38 weeks of gestation to the same mother and a different father from patient 1's. His birth weight was 2,405 g. He could control his head at 3–4 months, turn over at 6 months, and sit unassisted at 7–8 months. His motor development was delayed thereafter, and he walked unassisted at 1 year and 7 months. His mental development was normal. Because of a persistently unstable gait, he was hospitalized and examined at 5 years and 11 months. Physical examination revealed moderate muscle weakness in the proximal lower limb, but Gower's sign was negative. Deep tendon reflex was normal. No sensory disturbance or ataxia was recognized. Ankle joint contracture and foot deformity were absent.

The following examinations were performed at 5 years and 11 months of age. Serum transaminase and creatine kinase levels were normal. Brain and spinal MRI revealed no abnormal findings. Motor nerve conduction velocity and amplitude were within the normal limits (51.1 m/s, 4.6 mV for the right median nerve, 51.1 m/s, 9.9 mV for the right tibial nerve). Sensory nerve conduction velocity and amplitude were also within the normal limits (57.3 m/s, 28.4 uV for the right median nerve, 63.7 m/s, 9.6 uV for the right sural nerve). Needle electromyography of the anterior tibial muscle showed long high-amplitude discharges (3.5–4.0 mV, 10 ms) consistent with a neurogenic pattern, although no denervation potential, including positive sharp wave or fibrillation potential, was present, while the right biceps brachii showed inconclusive results. Muscle CT revealed severe atrophy and lipid degeneration, most predominantly in the bilateral quadriceps femoris. The upper limbs and distal lower limbs were not affected (Fig. 1).

The patient is now 12 years old and can walk unassisted but with a waddling gait. He has shown no further deterioration of motor function. Proximal lower limb weakness and wasting are evident, but the patient shows no upper limb weakness. No sensory disturbance or ataxia has been recognized.

Patient 3 Patient 3 is the mother of the two sibs. She is currently 50 years of age. No family history (except for her children) of neuromuscular disorders was noted. Until we examined the second sib, she had not been noted to have proximal lower limb muscle weakness. She did not recall her infantile development, and it was impossible to obtain further information. She graduated from a regular high school, married, and raised her children. She has not shown any neurological deterioration. She did not show a waddling gait, but had difficulty squatting. She was examined at 44 years of age. Her deep tendon reflex was normal, and no ankle joint contracture was present. Muscle CT revealed bilateral quadriceps-dominant muscle atrophy and lipid degeneration (Fig. 1). She also demonstrated mild muscle atrophy in her hip. Unfortunately, CT of the distal lower limb muscle could not be performed.

Exome sequencing

We performed the whole-exome sequencing of two patients (II-1 and II-2; Fig. 3a). Three micrograms of genomic DNA

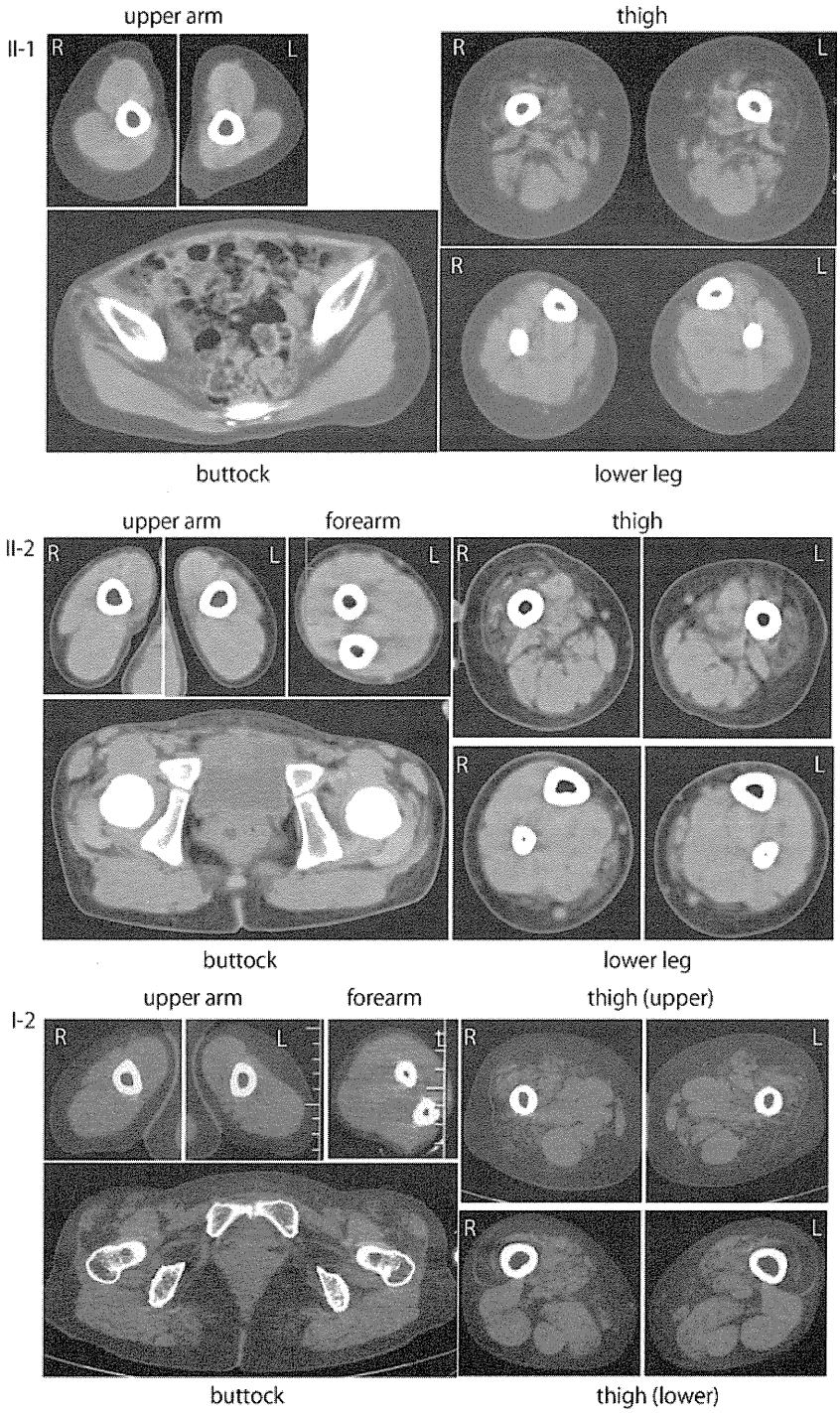

Fig. 1 Muscle imaging. Muscle computed tomography images of patient II-1 at the age of 3 years and 1 month (*upper*), patient II-2 at the age of 5 years and 11 months (*middle*), and patient I-1 at the age of 44 years (*lower*) are displayed. *R* right, *L* left

was processed using a SureSelect Human All Exon Kit v.1 (approximately 180,000 exons covering 38 Mb of the CCDS database) (Agilent Technologies, Santa Clara, CA) according to the manufacturer's protocol. Captured DNA was diluted to a concentration of 8 pM and sequenced on a Genome Analyzer IIx (Illumina, San Diego, CA) with 76-bp paired-end reads. We used two of the eight lanes in the flow cell (Illumina). Image analyses and base calling were performed by sequence control software real-time analysis and/or Off-line Basecaller software v1.6.0 (Illumina). Alignment was performed using CASAVA software v1.6.0. The quality-controlled (Path Filter) reads were mapped to the human reference genome (UCSC hg19, NCBI build 37), using mapping and assembly with quality (MAQ) and NextGENe software v2.0 (SoftGenetics, State College, PA). SNPs in MAQ-passed reads were annotated using the